Fast and selective interband transfer of ultracold atoms in bichromatic lattices permitting Dirac points

Tomotake Yamakoshi[1] and Shinichi Watanabe[2]

[1]*Institute for Laser Science, University of Electro-Communications, 1-5-1 Chofugaoka, Chofu-shi, Tokyo 182-8585, Japan*

[2]*Department of Engineering Science, University of Electro-Communications, 1-5-1 Chofugaoka, Chofu-shi, Tokyo 182-8585, Japan*

(Received 18 June 2018; published 24 January 2019)

An experimental group in Beijing [Yueyang Zhai *et al.*, Phys. Rev. A **87**, 063638 (2013)] introduced the method of the standing-wave pulse sequence for efficiently preparing ultracold bosonic atoms into a specific excited band in a one-dimensional optical lattice. Here, we report on a theoretical extension of their work to the problem of one-dimensional bichromatic superlattices in order to understand a wave packet shaping process in higher bands. Varying the lattice parameters leads to the so-called Dirac point where a pair of excited bands crosses. This paper thus discusses *simultaneously* efficient excitation of the wave packet to the proximity of the Dirac point and its subsequent dynamics in the force field of a parabolic trap. We numerically explore optimal pulse-sequence parameters and find an optimized sequence which excites more than 99% of the atoms in an ideal situation to the first and second excited bands within 100 μs. Our main finding is that the system permitting the Dirac point possesses a region of parameters where the excited energy bands become nearly parabolic, conducive to a robust wave packet with high coherence and isochronicity. We also provide an appropriate data set for future experimentation, including effects of the atom-atom interaction by way of the mean-field nonlinear term.

DOI: 10.1103/PhysRevA.99.013621

I. INTRODUCTION

Ultracold atoms and molecules in optical lattices have been eagerly investigated over the last 20 years. These quantum systems are suitable for simulating various Hamiltonian systems in the lattice, e.g., the Bose- and Fermi-Hubbard models [1]. Recent experiments demonstrated their high controllability and accessibility via Mott-superfluid transitions, quantum effects induced by artificial gauge fields, and so forth [2,3]. In recent years, unconventional phenomena in higher bands, e.g., topological effects, chiral superfluidity, and so forth, have attracted much attention with a view to developing new quantum technologies [4]. One of the intriguing topics is coherent wave packet preparation of a target state with high fidelity, e.g., the narrowing of the velocity spreading of the wave packet [5] and the rapid ground state loading onto the lattice [6], namely, techniques required for initializing quantum simulations. The present paper concerns manipulations of ultracold atomic wave packets, especially preparing higher band components with high fidelity in a highly tunable bichromatic one-dimensional lattice. Such techniques are desired for investigating low-dimensional quantum properties subject to a designed band structure.

The bichromatic lattices were experimentally realized in early 2000 [7], and there ensued examination of such phenomena as the Landau-Zener tunneling [8], Bloch oscillations [9], and Stückelberg interferometry of ultracold matter waves [10]. As for the energy bands, D. Witthaut *et al.* [11] theoretically suggested that the first and second excited bands would cross if experimental parameters were properly set so that the dynamics near the crossing could be mapped onto the Dirac equation, hence the coinage of the "Dirac point." This theoretical proposal was experimentally examined by T. Salger *et al.* [12]; they demonstrated the Landau-Zener transition at the Dirac point, also known as the Klein tunneling, subject to the optical dipole trapping and the gravitational potential. To this day, many groups have studied the bichromatic lattice system in terms of quasirelativistic properties [13], topological properties [14], and also in association with the time-wise lattice system [15], etc. Recently, Reid *et al.* reported a theoretical study on the manipulation of ultracold atoms in the bichromatic lattice using the Landau-Zener transition caused by a linear external potential [16]. Unfortunately, the theory falls short of achieving maximal coherence for shaping the wave packet, being based on the Bloch oscillation.

Coherent population transfer onto a specific band is a prerequisite for achieving coherent quantum control over a wide range of Hilbert space. The Aarhus group [17] and the Hamburg group [18] succeeded in conducting coherent manipulation by using an amplitude modulation of the optical lattice. This technique conserves energy and quasiomentum during an interband transition, thus it is suitable for the coherent wave packet shaping [19–21] and the band spectroscopy [22] although the transfer rate is rather low. On the other hand, an experimental group in Beijing demonstrated in 2013 [23] that a similar technique called the "standing-wave pulse sequence" was extremely efficient. This straightforward technique is discussed in an early experimental paper and is also known as bang-bang (on-off) control [24]. It repeatedly turns the optical lattice on and off and applies time-wise pulses of impulse to a confined Bose-Einstein condensation (BEC) with appropriate time intervals. In their first experimental paper, they demonstrated transfer from the ground

state to the second excited band (D band) with 99% fidelity. And they also achieved a 50%–50% superposition of the ground band (S band) and the second excited band. After this demonstration of the preparation process, this technique was applied to promote the wave packet into the fourth excited band (G band) to study the dynamics of ultracold atoms in the combination of an optical lattice and a harmonic trap [25]. Very recently, they demonstrated that the pulse sequence is also valid in two-dimensional (2D) and 3D systems [26] and performed a Ramsey interferometer using S and D bands [27].

In this paper, we study the coherent population transfer by the "standing-wave pulse sequence" method in the bichromatic optical lattice (OL). Because the Bloch states have an unconventional structure due to the Dirac points, the transition selection rule indeed becomes modified by the added OL of lattice periodicity $\lambda/4$ where λ is the laser wavelength. First, we theoretically study the Bloch bands and the transfer selection rule simply in the presence of the bichromatic OL or the monochromatic OL, but without any trap. We numerically simulate the preparation process with the time-dependent Schrödinger equation (TDSE) [28] in a condition realistic enough for subsequent simulation of the experiment [23] with the wave packet. We shall show that with the given condition, the population transfer of up to 90% to the first and second excited bands is attainable within 100 μs. The preparation time being too short for environmental noises to cause dephasing, the standing-wave pulse sequence method may as well be considered as highly reliable for setting up the desired wave packet.

We think it appropriate to present specific observables, keeping future experiments in mind. To this end, we show the momentum distributions that could be observed by band mapping [29] after following the postexcitation dynamics for a short while. We show that in the presence of the Dirac point, the energy dispersion curves of the first and second excited bands become nearly parabolic for realistic experimental parameters, thus the wave packet excited to the neighborhood of the Dirac point proves surprisingly robust and nearly isochronic. We analyze the wave packet dynamics by mapping it onto a semiclassical Hamiltonian [19–21].

Generally, the atom-atom interaction via the s-wave scattering is non-negligible, causing dephasing of the wave packet. In the treatment of ultracold atomic systems, the interaction is often represented by a nonlinear term in the framework of the mean-field approximation [30]. In addition to the dephasing, the strong nonlinear term modulates the band structure and Bloch waves [31], thus altering the wave packet dynamics in the OL. In order to examine this point in the context of this paper, we solve the time-dependent Gross-Pitaevskii equation [30] numerically with the nonlinear term inclusive thus providing information regarding realistic experimental parameters.

The paper is organized as follows. Section II outlines the theoretical model system. Section III analyzes numerical results of the excitation process and the subsequent dynamics caused by the external harmonic confinement. The effects of the nonlinear term will also be discussed. Section IV concludes the paper. Technical details are supplemented in the Appendixes.

II. MATHEMATICAL DEFINITION AND BASIC FEATURES OF THE SYSTEM

According to the experimental papers [23,25,29,32], ultracold atoms are initially loaded onto a 3D harmonic trap. Then, the 1D OL is turned on to shape the relative amplitudes of the Bloch states (on-duty cycle), and then it is turned off to induce relative phase shifts between bands (off-duty cycle). The net effect is the desired interband transition. These steps are repeated until the wave function $\Psi(t)$ reaches the target state Ψ_{target}.

Here, we consider the dynamics of interacting bosonic atoms in the bichromatic OL by solving the Gross-Pitaevskii equation [30]. Some notation and techniques used in this paper are available in our numerical studies presented in Refs. [19,20]. The 1D version of the system is described by the time-dependent Hamiltonian

$$H = -\frac{\hbar^2}{2m_a}\frac{\partial^2}{\partial x'^2} + \alpha(t)\{V_1 \sin^2(k_r x') + V_2 \sin^2(2k_r x')\} + \frac{1}{2}m_a\omega_0^2 x'^2 + g_{1D}N|\Psi(x')|^2,$$

where V_1 is the height of the optical lattice with the period of $\lambda/2$, V_2 is with the period of $\lambda/4$, $\alpha(t)$ equals 1 during an on-duty cycle, otherwise it is 0, ω_0 is the frequency of the harmonic trap, N is the number of total atoms, and g_{1D} parametrizes the effective atom-atom interaction contracted from 3D to one degree of freedom. We use recoil energy $E_r = \hbar^2 k_r^2/2m_a$ as the unit of energy, recoil momentum $k_r = 2\pi/\lambda$ as the unit of (quasi)momentum, lattice constant $\lambda/2$ as the unit of length, and rescaled time $t = E_r t'/\hbar$ as the unit of time. Here $\hbar$, λ, and m_a correspond to the Planck constant, laser wave length of the optical lattice, and atomic mass, respectively. Rescaling the Hamiltonian, we get

$$H = -\frac{\partial^2}{\partial x^2} + \alpha(t)\{s_1 \sin^2(x) + s_2 \sin^2(2x)\} + \nu x^2 + g|\Psi(x)|^2, \quad (1)$$

where x, s_1, s_2, and g denote $x = k_r x'$, $s_1 = V_1/E_r$, $s_2 = V_2/E_r$, and $g = g_{1D}N/E_r$ respectively. According to Ref. [33], $g_{1D} = \frac{4\hbar^2 a}{m_a a_\perp^2}(1 - 1.4603\frac{a}{a_\perp})^{-1}$, where a, $a_\perp = \sqrt{\frac{2\hbar}{m_a\omega_\perp}}$, and $\omega_\perp$ are the s-wave scattering length, effective transverse scattering length, and effective transverse trapping frequency, respectively. The atom treated here is ^{87}Rb whose s-wave scattering length is $a = 4.6 \times 10^{-9}$ m. Typically, the effective transverse frequency $\omega_\perp = 2\pi \times 10 - 2\pi \times 1000$ Hz and the number of atoms is 10^4–10^6, therefore g ranges from 10^{-5} to 1. The other parameters are the same as in Ref. [23]. We note that g could be made to vary from exact 0 to infinity by the Feshbach resonance [34]. However, we limit ourselves to a weakly interacting regime in this paper. We also note that the relative phase between the optical lattice of period $\lambda/2$ and that of $\lambda/4$ can be controlled experimentally; however, in this paper, we only consider the case of the relative phase equal to 0 for simplicity.

The unperturbed Bloch states $\{\phi_q^n(x)\}$ formed by the bichromatic OL part of H, namely, $H_B = -\frac{\partial^2}{\partial x^2} +$

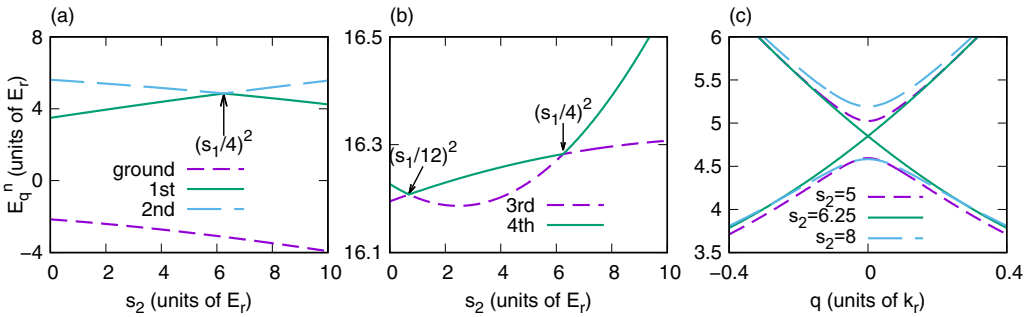

FIG. 1. (a) Ground (purple dashed), first (green solid), and second (light-blue long-dashed) excited band energies as a function of s_2 with $q = 0$ and $s_1 = 10$. The results are given by solving the recurrent equation of the bichromatic system [Eq. (3)]. The first and second excited bands cross at $s_2 = (s_1/4)^2 = 6.25$. (b) Third (purple dashed) and fourth (green solid) excited band energies as in (a). In addition to the crossing at $s_2 = (s_1/4)^2$, they cross at $s_2 = (s_1/12)^2$. (c) Lattice height s_2 dependence of the band structure around the crossing of the first and second excited bands. As shown in (a), the crossing or the Dirac point [11,12] happens when $s_2 = 6.25$.

$\{s_1 \sin^2(x) + s_2 \sin^2(2x)\}$ may be expanded as

$$\phi_q^n(x) = e^{iqx} \sum_K C_B(n, q, K) e^{2iKx}, \tag{2}$$

where q is the quasimomentum, $n \in \mathbb{N}$ is the band index, $K \in \mathbb{Z}$ is the reciprocal vector index so that the coefficient $C_B(n, q, K)$ obtains by solving the recurrent formula

$$\begin{aligned}(q + 2K)^2 C_B(n, q, K) - s_2 C_B(n, q, K - 2)/4 \\ - s_1 C_B(n, q, K - 1)/4 - s_1 C_B(n, q, K + 1)/4 \\ - s_2 C_B(n, q, K + 2)/4 \\ = \left(E_q^n - s_1/2 - s_2/2\right) C_B(n, q, K),\end{aligned} \tag{3}$$

namely, the central equation (see, for instance, the section on the energy bands in [35]) where E_q^n represents the eigenenergy of the Bloch state. In this paper, we use $n = 0$ as an index of the ground band.

Once the coefficients are obtained by diagonalization within an appropriately truncated K space, it immediately allows us to calculate the wave function at the completion of the on-duty cycle or the off-duty cycle. To be explicit, $\Psi(\tau_1) = \sum_{n,q} e^{-iE_q^n \tau_1} \langle \phi_q^n \,|\, \Psi(t = 0) \rangle$ or $\Psi(\tau_1 + \tau_1') = \sum_K e^{-4iK^2 \tau_1'} \langle e^{2iKx} \,|\, \Psi(\tau_1) \rangle$, where $\Psi(t = 0)$ is the initial condition [24]. This method applies repeatedly to any length of pulse sequence. The time durations τ_1 and τ_1' could be numerically optimized. In this paper, we used brute force to search optimal values of τ_1 and τ_1' with a 0.1-μs step size in each of them ($0 \leqslant \tau_1,\ \tau_1' \leqslant 40\ \mu$s).

Before presenting the numerical results, we note that parity plays an important role in excitation processes for atoms in a monochromatic optical lattice as noted in the experimental papers [23,25]. Here we assume that the initial condition is a zero momentum state which is appropriate for weak parabolic trap system. This assumption allows us to consider the dynamics at $q = 0$ only. In this case, the parity of the initial state is symmetric in K space, $\langle \phi_q^n \,|\, \Psi(0) \rangle = 0$ when the ϕ_q^n is antisymmetric so that the on-duty cycle does not change the parity. Thus the excitation to the antisymmetric states is prohibited. For the monochromatic OL, the Bloch states at $q = 0$ with even (odd) n are symmetric (antisymmetric), therefore a phase-modulated pulse sequence is needed to populate odd bands [25]. More detailed discussions with a toy model for the excitation process are given in Appendix A.

This intuitive explanation is certainly valid for the case of the bichromatic OL as well. Here we discuss the parity selection rule briefly while further details of the energy structure are discussed in Appendix C from the viewpoint of Bloch's theorem, somewhat differently from the previous study [11]. Figure 1 shows the energy structure as a function of s_2 for $q = 0$ with s_1 fixed to 10. The energy difference between the first and second excited bands decreases as s_2 is increased until $s_2 = (s_1/4)^2$ where it vanishes. Meanwhile, the selection rule is modified due to the symmetry of the Bloch states. The parity of the first and second excited bands interchanges across this crossing (see Fig. 2), which prevents the wave packet from reaching the second excited band from below by this manipulation.

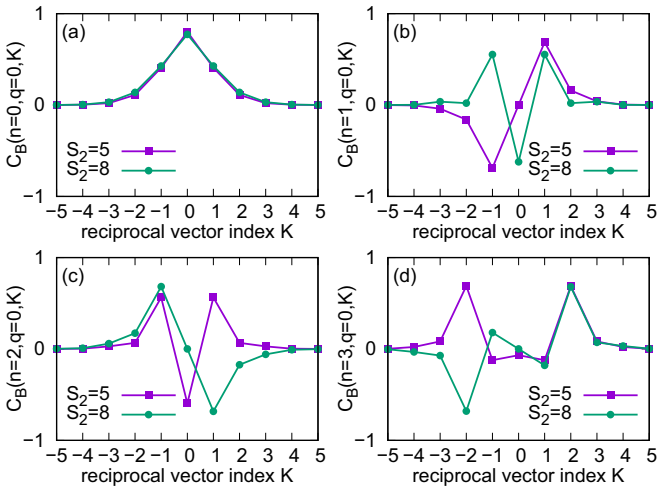

FIG. 2. Bloch coefficient $C_B(n, q, K)$ as a function of K as in Figs. 11(a) and 11(b) of Appendix A. Purple squares show the results of $s_2 = 5$ and green circles those of $s_2 = 8$. Panels (a)–(d) correspond to the ground through the third excited bands. Note $s_2 = 5$ of (b) corresponds to $s_2 = 8$ of (c) up to sign, and likewise for $s_2 = 8$ of (b) and $s_2 = 5$ of (c).

III. NUMERICAL RESULTS

The experimental work of [23] employed a set of numerically optimized laser pulse parameters to attain a large target population. The present work extends this approach to the bichromatic OL system. Moreover, it takes into account effects of the nonlinear term incurred by the atom-atom interaction as well as the acceleration due to the harmonic trap potential. All the numerical results below are obtained by solving the time-dependent Schrödinger equation (TDSE), namely, $i\frac{d}{dt}\Psi(t) = H\Psi(t)$ with the Hamiltonian in Eq. (1). In general, *fidelity* is evaluated as $F(t) = |\langle\Psi_{\text{target}}|\Psi(t)\rangle|^2$ from the solution $\Psi(t)$. However, we evaluate in this paper, as a more informative index, the band population $B_n(t) = \sum_q |\langle\phi_q^n|\Psi(t)\rangle|^2$ which can be evaluated by the experimental band mapping technique. In solving the TDSE, we fix $s_1 \equiv 10$ throughout the rest of the paper, and focus on the range $s_2 = 5$–8 containing $s_2 = 6.25$ at which the crossing of interest occurs.

A. Excitation by OL pulse sequence

Let us consider excitation of the initial wave packet. First, we ignore the harmonic trap and the atom-atom interaction for simplicity. The initial state is in the zero momentum state, i.e., $q = 0$ as discussed earlier. Even under this simplification, the issue of finding the optimized pulse sequence is nontrivial, being intrinsically a multiple-minimum problem since the excitation rate depends sensitively on the pulse duration. Stated differently, population of the target band sweeps through numerous local optima as the pulse parameters are varied smoothly, but finding the absolute maximum is difficult. See Appendixes A and B for details.

The second optical lattice of the bichromatic OL plays the role of interchanging the Bloch coefficients (up to sign) across the Dirac point as noted in Fig. 2. This implies that a pulse sequence cannot excite the atoms to the first excited band while $s_2 < s_1^2/16$, but the tendency changes abruptly across the critical value $s_2 = 6.25$, that is, the process fails to excite them to the second excited band once s_2 exceeds 6.25 (recall the parity interchange in Sec. II).

Table I shows sets of optimal parameters for several values of s_2 while s_1 is fixed to 10. It clearly demonstrates the interchange at $s_2 = 6.25$ as described above. In all the cases presented, the applied sequences succeed in preparing almost 100% of the atoms into either of the two excited bands.

TABLE I. Band population at several values of s_2 for given cycle parameters in the bichromatic OL with lattice height s_1 fixed to 10.

s_2	τ_1	τ_1'	τ_2	τ_2'	$B_1(\tau_{\text{total}})$	$B_2(\tau_{\text{total}})$
5	3.8	4.9	23.1	28.9	0.000	0.999
6	21.4	30.8	8.4	9.8	0.000	0.999
6.25	21.6	30.5	8.7	10.0	0.479	0.520
7	21.4	30.0	8.7	11.2	0.998	0.000
8	13.0	22.9	2.5	30.4	0.995	0.001

Turning to the trap ignored thus far, we note that in the Beijing experiment an atomic BEC is set up in a 3D harmonic trap first. The initial wave packet then has a Gaussian distribution of finite width in momentum space. To see the effect of the trap, we plot in Fig. 3 the population transfer rate $R_0(q)$ calculated without a trap as a function of quasimomentum using the cycle parameters shown in Table I. The shape of the excited wave packet at the pulse sequence's end could then be estimated by this transfer rate $R_0(q)$ times the initial quasimomentum distribution $\rho(q)$ integrated over q, i.e., $\int R_0(q)\rho(q)\,dq$. The rate $R_0(q)$ being close to 1 around $q = 0$ (Fig. 3), the initial wave packet localized at $q = 0$ would indeed be ideal for selective momentum transfer. In Table II, we show the first and second excited band population at the pulse end with $\nu = 1.0 \times 10^{-5}$ ($2\pi \times 20$ Hz) and $\nu = 1.2 \times 10^{-4}$ ($2\pi \times 70$ Hz). These representative data suggest that the harmonic trap is non-negligible and delocalizes the excited wave packet in momentum space, reducing the transfer rate $R_0(q)$ in comparison to the trapless case. For instance, in Table II as we look at the $n = 2$ component, the transfer rate is 91% at $\nu = 1.0 \times 10^{-5}$ whereas it is 81% at $\nu = 1.2 \times 10^{-4}$ [Figs. 3(a) and 3(c)]. Thus, the pulse sequence with a tight harmonic trap may not be advisable for selective momentum transfer.

Interestingly, Fig. 3 shows that the transfer rate becomes rather flat, i.e., less q dependent as s_2 exceeds 6.25. Indeed as shown in Table II, the reduction rate is $0.808/0.912 = 0.886$ for the second excited band with $s_2 = 5$, and

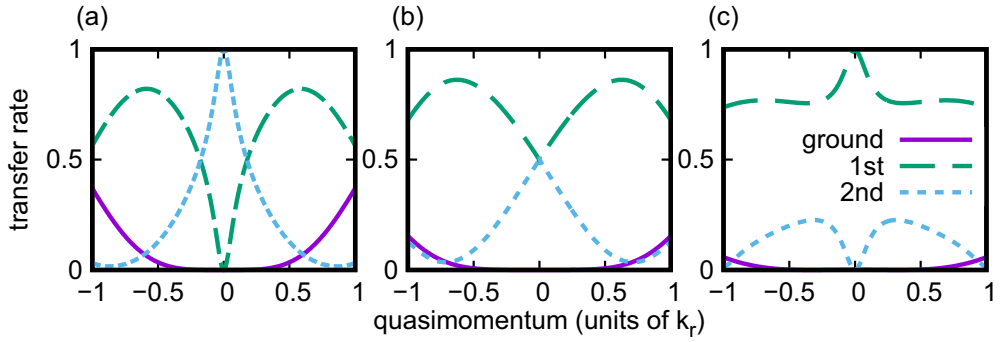

FIG. 3. Population transfer rate as a function of quasimomentum with the cycle parameters shown in Table I. (a), (b), and (c) correspond to $s_2 = 5$, 6.25, and 8. Purple solid, green long dashed, and light-blue short dashed lines show ground, first, and second excited bands, respectively. In (a), the distributions have a sharp peak (kink) for second (first). As the lattice height s_2 increases toward (c), the peak and the kink in (a) flip over, making the distribution seemingly less q dependent. See text for more detail.

TABLE II. First and second excited band populations at the end of the pulse sequence with $s_1 = 10$.

	$s_2 = 5$		$s_2 = 6.25$		$s_2 = 8$	
ν	$n = 1$	$n = 2$	$n = 1$	$n = 2$	$n = 1$	$n = 2$
1.0×10^{-5}	0.084	0.912	0.550	0.443	0.953	0.037
1.2×10^{-4}	0.186	0.808	0.585	0.400	0.897	0.088

$0.897/0.953 = 0.941$ for the first excited band with $s_2 = 8$. In contrast to its importance in shaping the initial wave packet, the harmonic trap is much less significant during excitation since the duration of 100 μs is much shorter than the period of motion in the trap which is about several milliseconds.

B. Postexcitation dynamics with the harmonic trap

Experimentally, the dynamics in quasimomentum space is studied by applying the band mapping technique [17,18,29] to excited components. In this technique, the atoms are released adiabatically after a given holding time during which both the OL and harmonic potential are kept on, and then their momenta are measured by the time-of-flight method (see Fig. 1 of Ref. [29]). We replicate the experimental situation of the Hamburg group [18–20] in our 1D calculations and examine the dynamics of the excited wave packet in quasimomentum space, quantum mechanically as well as semiclassically.

First, let us analyze the dynamics from the semiclassical viewpoint; the wave packet obeys

$$H_{\rm cl} = E_q^n + \nu x^2, \tag{4}$$

under the single-band approximation. This semiclassical Hamiltonian allows us to calculate the outermost location of the excited wave packet $x_{\rm max}$ and the critical time τ_c needed for the wave packet to reach the edge q_0 of the excited band, where $q_0 = 0$ for even-indexed bands and 1 for odd-indexed ones. Here we assume that the excited wave packet is initially located at $(x_i, q_i) = (0, \nu^{1/4}/\sqrt{2})$, where the representative value of q_i corresponds to the variance of the ground-state wave function in momentum space, and that the shape does not change during the pulse sequence. This leads to the following semiclassical expressions: $x_{\rm max} = \pm\sqrt{\frac{E^n_{q_i} - E^n_{q_0}}{\nu}}$ and $\tau_c = \frac{1}{2\sqrt{\nu}} \int_{q_0}^{q_i} (\sqrt{E^n_{q_i} - E^n_q})^{-1} dq$.

This single-band approximation breaks down when the Dirac point appears as in Fig. 1(c). The motion of the wave packet in the region covering the Dirac point is best analyzed with the aid of the extended zone representation suitable for the $\lambda/4$ OL. To a good approximation, the band energy dispersion is given by the tight-binding model [35], namely, $E(q_{\rm ext}) = A - \sum_{m=1}^{\infty} 2J_m \cos(m\pi q_{\rm ext}/2)$ for the first ($|q_{\rm ext}| \leqslant 1$) and second ($1 \leqslant |q_{\rm ext}| \leqslant 2$) excited bands, where A and J_m are the energy offset and the mth order hopping constant, respectively. The energy dispersion could be expanded into Taylor series with respect to $q_{\rm ext}$ as $E(q_{\rm ext}) = A - 2\sum_{m=1}^{\infty} J_m + \frac{\pi^2 q_{\rm ext}^2}{4} \sum_{m=1}^{\infty} m^2 J_m - \frac{\pi^4 q_{\rm ext}^4}{192} \sum_{m=1}^{\infty} m^4 J_m + \cdots$. In the limit of $s_1 \gg 1$ while holding $s_2 = (s_1/4)^2$, the tight-binding energy dispersion reduces to a single cosine function. In contrast, it goes to a superposition of cosine terms in the limit of $s_1 \ll 1$ [35]. As shown in Fig. 4, there is a region between these two limits where the dispersion approaches a parabolic function due to the destructive interference of cosine terms. In the case of $s_1 = 10$, this effect suppresses the higher-order terms so that the classical Hamiltonian can be well approximated by $H_{\rm cl-ext} = (\sum_{m=1}^{\infty} \pi^2 m^2 J_m) q_{\rm ext}^2/2 + \nu x^2$, which is quadratic both in x and $q_{\rm ext}$, making the excited wave packet robust. The wave packet thus enjoys isochronicity to an unexpectedly high degree. Moreover, the dispersion near the Dirac point is approximately given by $E(q) = A - \pi J_1 q$ in the limit of $s_1 \gg 1$ where $q = q_{\rm ext} \pm 1 \sim 0$ is the quasimomentum in $E(q_{\rm ext})$ expressed above in the *reduced zone* representation. This dispersion is thus in line with the explanation by the Dirac equation [11,12].

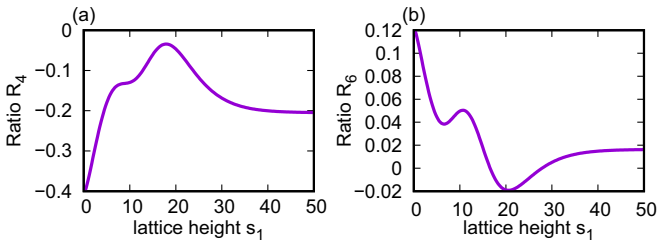

FIG. 4. Ratio of (a) quartic term to quadratic $R_4 = \frac{\pi^2}{48} \frac{\sum_{m=1}^{\infty} m^4 J_m}{\sum_{m=1}^{\infty} m^2 J_m}$ and (b) sextic to quadratic $R_6 = \frac{\pi^4}{5760} \frac{\sum_{m=1}^{\infty} m^6 J_m}{\sum_{m=1}^{\infty} m^2 J_m}$. In the limit of $s_1 \gg 1$, $|R_4|$ goes to 0.206 and $|R_6|$ goes to 0.017, which are rather small.

Let us look at some numerical results of the TDSE calculations. Figure 5 shows the postexcitation evolution of the wave packet during the holding time. Here the parameters are $\nu = 1.0 \times 10^{-5}$, $s_1 = 10$, and $s_2 = 5$ for (a), $s_2 = 6.25$ for (b), and $s_2 = 8$ for (c), respectively. In the case of (a), most of the atoms are transferred to the bottom of the second excited band, and only a small fraction of the wave packet goes to the top of the first excited band. In addition, the Landau-Zener transition between first and second excited bands is negligible [19,36]. The atoms are thus trapped in the second excited band. In the case of (b), the gap is closed. Therefore, the wave packet traces the band structure without reflection at the edge of the second excited band. This results in the well-defined sharp wave packet in position space. In the case of (c), the wave packet traces the first excited band, and their typical wave packet motion is characterized by $x_{\rm max} = 117$ lattice sites and $\tau_c = 11.9$ ms. We note that all the figures show some beats, which are characteristic interference patterns. This effect is due to the nonparabolic dispersion of the band structure and the broadening of the initial wave packet in momentum space.

Figure 6 shows momentum distributions after the band mapping procedure is effected at representative values of the holding time. (Note we plot only the positive part of the momentum space because the density distribution always keeps its symmetric feature with respect to $q = 0$.) We employ the same band mapping procedure as in the experimental paper [29], namely, we let the lattice height decay with the decay time constant equal to 100 μs so that the band mapping is presumably completed in 1 ms. The resulting distribution is what would be observed experimentally. As we discussed above, the momentum distribution is almost localized around $p = 2$ in Fig. 6(a). However, in Figs. 6(b) and 6(c) the

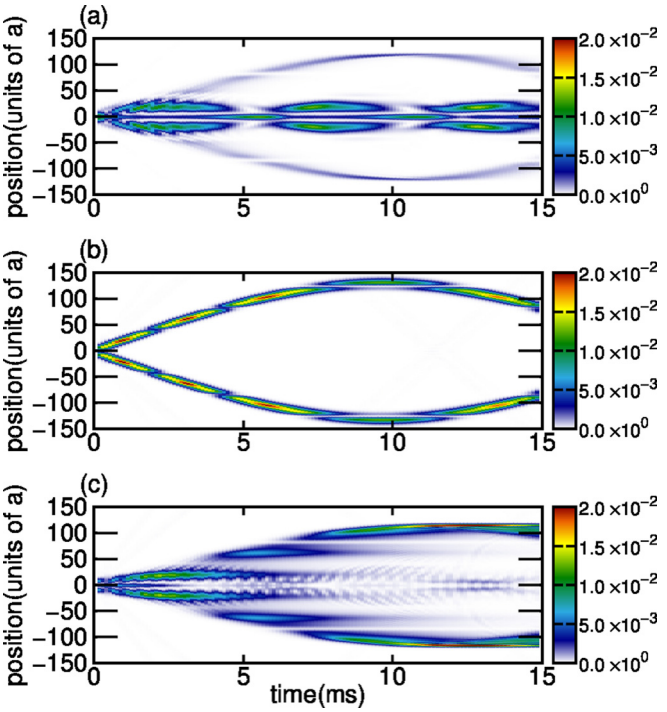

FIG. 5. Time evolution of the wave packet in position space as a function of holding time with $s_1 = 10$ and $\nu = 1.0 \times 10^{-5}$. Time $t = 0$ corresponds to immediately after the second off-duty cycle. Density becomes denser toward red and lower toward white. (a) For $s_2 = 5$, the excited wave packet is mostly located around the bottom of the second excited band, thus it is located around the origin of the harmonic potential. (b) For $s_2 = 6.25$, the band gap becomes closed, therefore the excited wave packet smoothly traces the band structure. This results in a less dispersive motion of the wave packet in position space. (c) For $s_2 = 8$, the excited wave packet gets located around the top of the first excited band, therefore it traces the first energy band. The wave packet can thus travel far away from the origin.

main part of the momentum distribution travels in the first excited band $1 < p < 2$. Especially, in Fig. 6(b), the wave packet appears less dispersive than the other two cases, the classical Hamiltonian being well approximated by that of the 1D harmonic trap.

Let us also examine the dynamics (Fig. 7) with a tighter harmonic trap $\nu = 1.2 \times 10^{-4}$. In this case, the initial wave

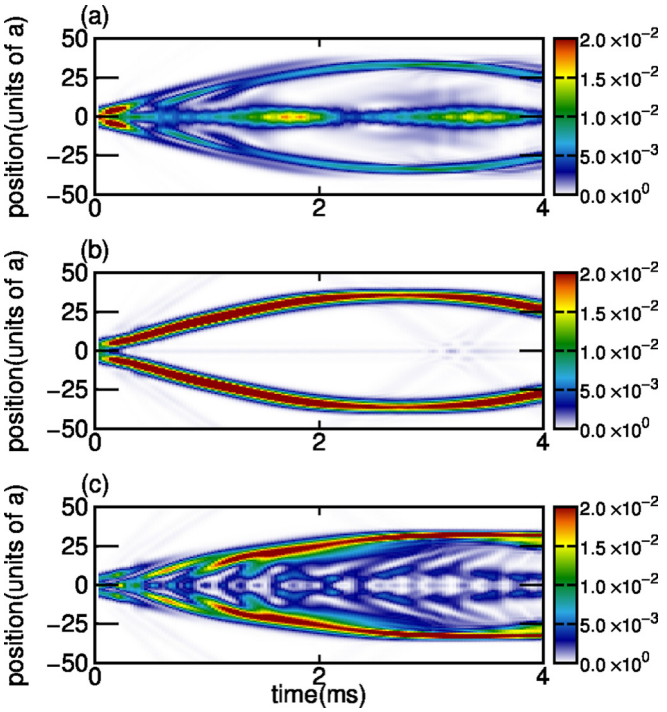

FIG. 7. Time evolution of the wave packet in position space as a function of holding time. Same as Fig. 5 with $\nu = 1.2 \times 10^{-4}$.

function has a broader momentum distribution than in the previous looser case. The features are almost the same as in the case of $\nu = 1.0 \times 10^{-5}$; however, the tighter trap reduces both the time scale of the periodic motion and the length scale of the position space. In Fig. 7(c), the characteristic values are $x_{\max} = 33$ lattice sites and $\tau_c = 3.13$ ms. Figure 8 also shows the momentum distribution after the band mapping. In comparison to Fig. 6, each momentum distribution shows a broader shape, reflecting the spatial tightness of the initial wave function.

C. Effects of the atom-atom interaction

One of the reasons why ultracold atomic systems are considered to offer a fascinating experimental playground is that the strength of the nonlinear interaction is controllable by the Feshbach resonance [34] so that the strongly interacting

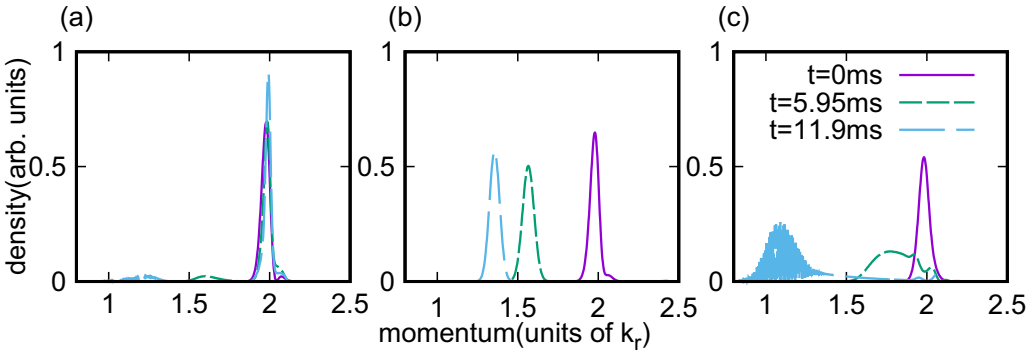

FIG. 6. Momentum distributions after the band mapping procedure with holding time $t_{\text{hold}} = 0$ (purple solid), 5.95 (green dashed), and 11.9 (light-blue long-dashed) ms. Here $\nu = 1.0 \times 10^{-5}$. (a) corresponds to $s_2 = 5$, (b) to $s_2 = 6.25$, and (c) to $s_2 = 8$.

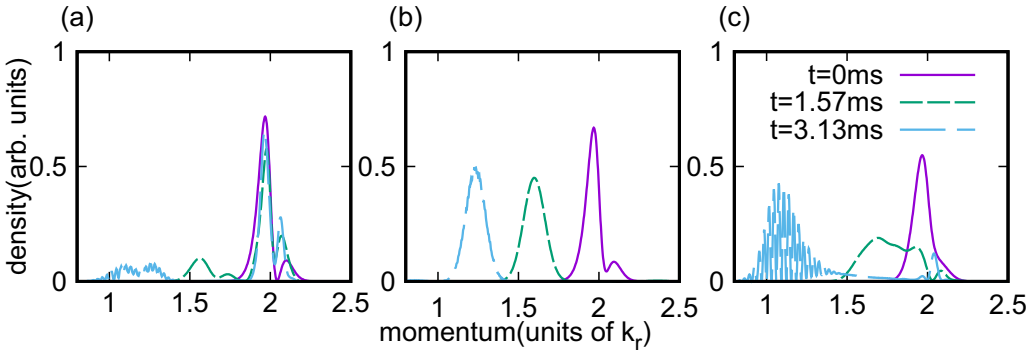

FIG. 8. Same as Fig. 6 for $\nu = 1.2 \times 10^{-4}$. The holding time $t_{\rm hold} = 0$, 1.57, and 3.13 ms.

regime becomes experimentally accessible with ease. According to previous studies, the atom-atom interaction alters the conventional band structure, causing, for instance, the so-called nonlinear Bloch bands presenting loop-like structures at the band edge [30], solitary wave packets [31], and so forth. Such changes show up when the strength of the nonlinear term becomes comparable to the lattice height [37]. In the experimental system considered, the nonlinear term is typically quite small such as 10^{-5}–10^{-2}. Nevertheless, to make the influence of the nonlinear term clearly visible, we extend its numerical range from 0 up to 1 in this paper.

Figure 9 shows the time evolution of the *isochronic* wave packet after the pulse sequence at various values of the effective interaction g. For this reason, we use the same parameter set as for Fig. 5(b), but with (a) $g = 5 \times 10^{-4}$, (b) 1×10^{-2}, and (c) 1. Even in the case of (c) with $g = 1$, there is no dramatic change; therefore the system is insensitive to the interaction strength in a practical parameter regime. Nevertheless, the nonlinear term broadens the initial wave packet in space to such an extent that we notice the slight spatial broadening of the excited wave packet in Fig. 9(c) by scrutiny. On the contrary, in momentum space, the nonlinear term contracts the initial wave packet, therefore the excited wave packet immediately after the pulse sequence shows a narrower distribution as shown in Fig. 10(a). However, the wave packet with $g = 1$ spreads out gradually in momentum space due to the interaction which imparts momentum to the atom [Fig. 10(b)], so that the wave packet catches up with those for smaller values of g, and the distributions thus coincide after 11.9 ms. The semiclassical treatment then becomes adequate. This result indicates that the nonparabolic dispersion dominates the early dynamics in the parabolic lattice with $\nu = 1.0 \times 10^{-5}$. At any rate, it appears difficult for real experiments to reveal clear indication of the nonlinearity.

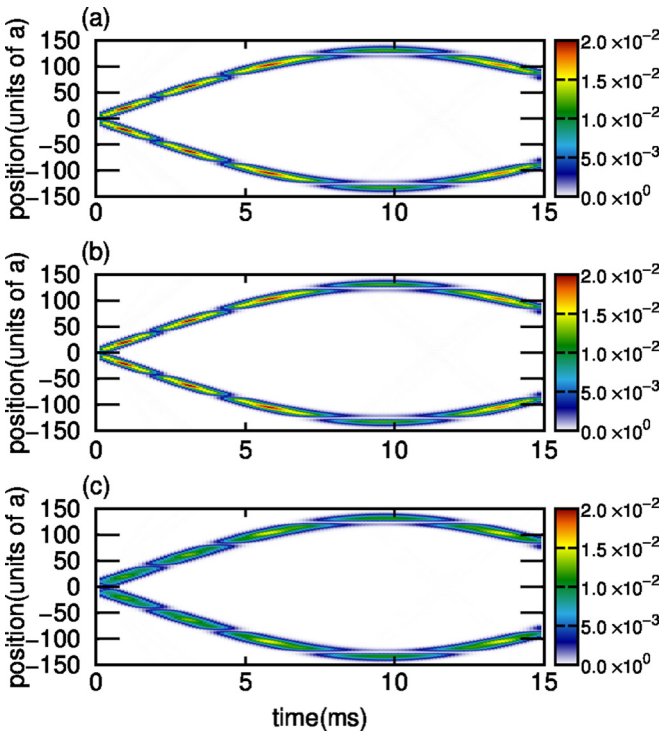

FIG. 9. Time evolution of the isochronic excited wave packet in position space as a function of holding time with (a) $g = 5 \times 10^{-4}$, (b) 1×10^{-2}, and (c) 1. Here $s_1 = 10$, $s_2 = 6.25$, and $\nu = 1.0 \times 10^{-5}$. All the cases show clear and robust oscillation as in Fig. 5(b).

IV. CONCLUSIONS

We have theoretically examined the standing-pulse wave sequence method established in Ref. [23], and extended it to the coherent wave packet shaping in higher bands of the one-dimensional bichromatic superlattice system. The bichromatic OL studied here revealed an unconventional crossing of energy bands, namely, the Dirac point, between the first and second excited bands. The excitation selection rule is seen to change abruptly across the Dirac point as the height of the second optical lattice is varied because the parity of the Bloch states changes correspondingly. Our numerical results show that the standing-wave pulse sequence method is also valid for the bichromatic optical superlattice. For an ideal set of parameters, the population transfer from the ground band to the first and second excited bands is attained within 100 μs with almost 100% efficiency.

In addition, we numerically examined effects of the harmonic trap and the atom-atom interaction. We mainly focused on the dynamics of the excited wave packet after the pulse sequence. In so doing, we identified momentum distributions of the excited wave packet by mimicking the experimental band mapping technique, namely, by simulating the adiabatic decay of the applied optical lattice.

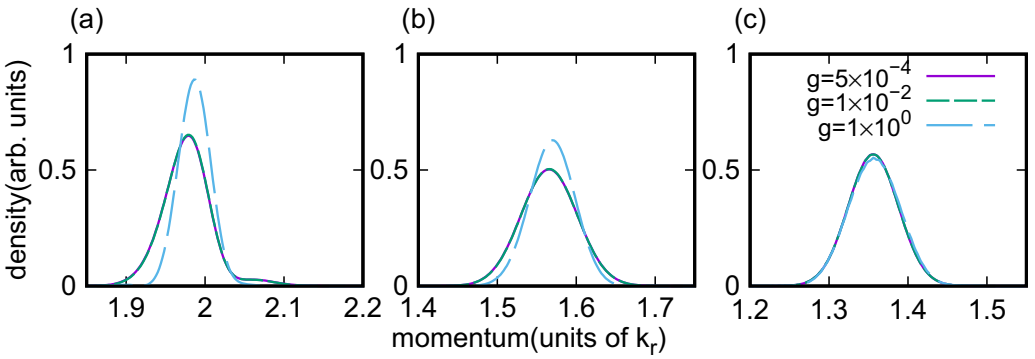

FIG. 10. Momentum distributions after the band mapping process with holding time (a) $t = 0$, (b) 5.95 ms and (c) 11.9 ms. See text for details.

The classical theory accounts for the bulk of the dynamics in phase space. We have seen that the band dispersion dominates the dynamics. We found that the band dispersion approaches a parabolic curve in the presence of the Dirac point, particularly with $s_1 = 10$. Consequently, the wave packet preparation in the presence of the Dirac point produces amazingly robust wave packets as shown in Figs. 5(b) and 7(b). This inspiring feature of the wave packet would be useful for atomic interferometry. We calculated the momentum distribution of the isochronic wave packet as a reference for future experiments.

The harmonic potential affects the width of the initial distribution in momentum space, which in turn causes some reduction of the transfer rate. This fact suggests that a low-frequency harmonic trap would be more preferable to a high-frequency one for preparing the initial state of the BEC. We also examined the effect of the atom-atom interaction in the framework of the mean-field theory which is sufficient for modeling practical experiments. We found that the interaction does not alter the dynamics substantially for the interaction strength considered. Since we merely considered the 1D system in this paper, it remains to explore how the dimensionality of the system affects the excitation process. However, its effect would be negligible in practical situations according to our previous study [20] as long as the nonlinear term is relatively small in comparison to the lattice height.

Compared to the amplitude modulation method [17,18], the pulse-sequence method excites atoms into higher bands in a shorter period of time with higher efficiency. Moreover, the acceleration by an external potential could serve to control the position of an atom initially localized in momentum space. Thus, creating solitary wave packets in the presence of the Dirac point would be an especially fascinating application akin to optical soliton generations in the field of quantum optics. Another fascinating application would be to investigate the topological dynamics in higher bands such as the topological pumping [38]. However, the pulse-sequence method may not be suitable for the selective momentum transfer which requires energy conservation. For instance, the hole creation in Fermionic quantum degenerate gases of Refs. [18,22] used the amplitude modulation method instead to guarantee energy conservation. On the other hand, devising a suitable combination of the pulse-sequence and the amplitude modulation would lead to a powerful strategy for precise and coherent manipulation of the atomic wave packet. Moreover, the combination may pave the way to the physics of exotic coherent resonant band couplings [3,39] with lattice modulation [21,40], lattice shaking [41], and so forth. Much remains to be explored.

ACKNOWLEDGMENTS

We thank T. Hosaka for his help with generating some preliminary numerical data sets. This work was supported by Research and Educational Consortium for Innovation of Advanced Integrated Science (CIAiS) and JSPS KAKENHI Grant No. JP17K05596.

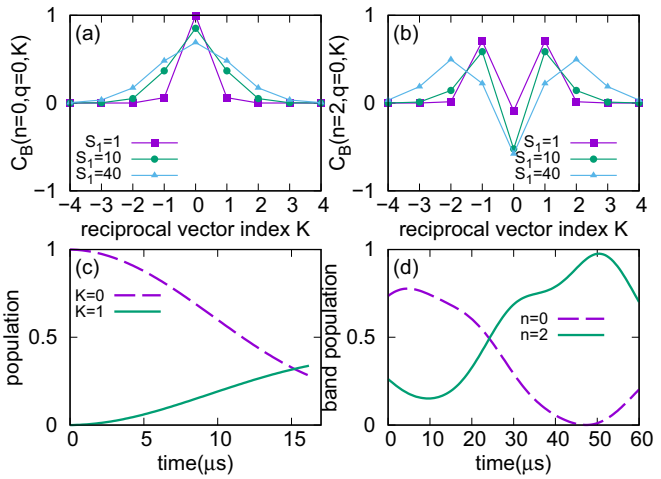

FIG. 11. Coefficients $C_B(n, q, K)$ for Bloch states at $q = 0$ (a) for the ground band and (b) for the second excited band. The horizontal axis represents reciprocal vector index K. Purple squares, green circles, and light-blue triangles show the results of $s_1 = 1$, 10, and 40, respectively. Especially, the toy model appropriate to $s_1 = 10$. (c) Populations of $K = 0$ (purple dashed) and $K = \pm 1$ (green solid) components during on-duty cycle with $s_1 = 10$. The on-duty process is halted at $t = \tau_1 = 16.2$ μs. (d) Band populations of $n = 0$ (purple dashed) and $n = 2$ (green solid) components during off-duty cycle with $s_1 = 10$ after the first on-duty cycle. The second excited band population reaches its maximum around $t = \tau_1' = 50.4$ μs.

APPENDIX A: TOY MODEL FOR THE PULSE-SEQUENCE METHOD

To grasp the mechanism of interband transition by the pulse-sequence method, here we account for the population transfer to the second excited band subject to a single standing-wave pulse sequence. Consider the following toy model for a monochromatic OL, namely, $s_2 = 0$ in Eq. (3), assuming the initial wave packet to be in the ground state of a very loose parabolic trap $v \simeq 0$. The system is spatially so spread out that the uncertainty principle demands $p_x = 0$, that is $K = 0$ with $q = 0$ [23]. The model consists of three states, $K = 0, \pm 1$ with $q = 0$ so that a state vector is represented by a triplet of numbers (a, b, c) such as

$$(a, b, c) \to ae^{-2ix} + b + ce^{2ix}.$$

The initial state is then

$$\Psi(t = 0) = (0, 1, 0),$$

while the normalized eigenvectors v_n $(n = 0, 1, 2)$ are

$$v_n = (C_B(n, 0, -1), C_B(n, 0, 0), C_B(n, 0, +1)),$$

where n is the band index. [See Figs. 11(a) and 11(b).] Turning the OL on suddenly is equivalent to projecting onto the OL eigenvectors, thus

$$\begin{aligned}\Psi(t = 0) &= \langle v_0|(0, 1, 0)\rangle v_0 + \langle v_2|(0, 1, 0)\rangle v_2 \\ &= C_B(0, 0, 0)v_0 + C_B(2, 0, 0)v_2.\end{aligned}$$

Propagating Ψ over the on-duty period τ_1, and then propagating over the off-duty period τ_1', we get, in column vector representation for clarity,

$$\Psi(t = \tau_1 + \tau_1') = \begin{pmatrix} \{C_B(0,0,0)C_B(0,0,-1)e^{-iE_0^0\tau_1} + C_B(2,0,0)C_B(2,0,-1)e^{-iE_0^2\tau_1}\}e^{-i4\tau_1'} \\ C_B(0,0,0)C_B(0,0,0)e^{-iE_0^0\tau_1} + C_B(2,0,0)C_B(2,0,0)e^{-iE_0^2\tau_1} \\ \{C_B(0,0,0)C_B(0,0,1)e^{-iE_0^0\tau_1} + C_B(2,0,0)C_B(2,0,1)e^{-iE_0^2\tau_1}\}e^{-i4\tau_1'} \end{pmatrix}.$$

This wave packet becomes proportional to v_2 if

$$\begin{aligned}f(\tau_1, \tau_1') = &\left[C_B(0,0,0)C_B(0,0,1)e^{-iE_0^0\tau_1} + C_B(2,0,0)C_B(2,0,1)e^{-iE_0^2\tau_1}\right]e^{-i4\tau_1'}C_B(2,0,0) \\ &- \left[C_B(0,0,0)C_B(0,0,0)e^{-iE_0^0\tau_1} + C_B(2,0,0)C_B(2,0,0)e^{-iE_0^2\tau_1}\right]C_B(2,0,1) = 0.\end{aligned}$$

The density $|f(\tau_1, \tau_1')|^2$ is doubly periodic in the present three-state model, thus a typical unit cell appears as in Fig. 12. Even under this simple assumption, the second excited band population is observed to reach 99% for $s_1 = 10$ as shown in Fig. 11(c) and 11(d). To summarize, the first on-off duty cycle attains minima of $|f(\tau_1, \tau_1')|^2$ through the phase difference between the $K = 0$ and $K = \pm 1$ components, and then in the actual experimental system, the second cycle is applied to make further optimization. In the general case, the multidimensional density plot as a function of $(\tau_1, \tau_1', \tau_2, \tau_2', \dots)$ reveals a multitude of minima, thus computational cost for optimization diverges as the number of pulse sequences increases. This problem may be optimizable, say, by the machine learning method.

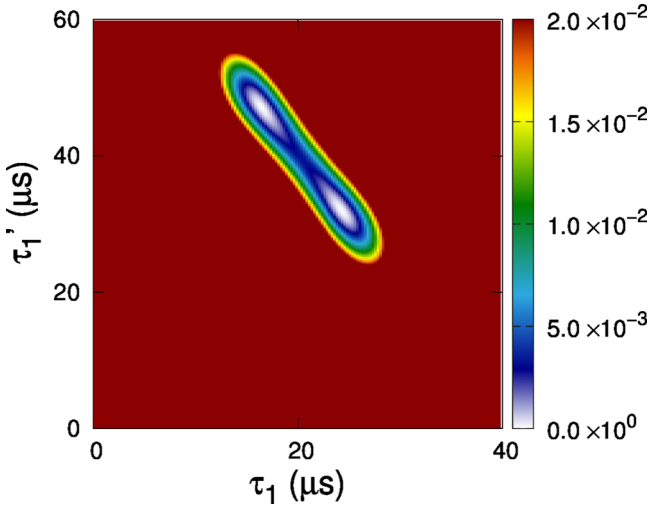

FIG. 12. Doubly periodic density $|f(\tau_1, \tau_1')|^2$ over a typical cell with a pair of minima. The shortest and most efficient procedure can be obtained by evaluating the total time $\tau_1 + \tau_1'$ and the density $|f(\tau_1, \tau_1')|^2$ from the figure.

APPENDIX B: OPTIMAL VALUES FOR THE MONOCHROMATIC OL SYSTEM

Here we validate our numerical approach by comparing with the experimental results of Ref. [23] for the monochromatic OL pulse sequence. As in Sec. III A, we assume absence of both harmonic trap and atom-atom interaction,

TABLE III. Parameter sets for monochromatic OL listed for $s_1 = 10$ and 20. Here τ_i and τ_i' represent the on-duty period and off-duty period, respectively, for the ith cycle $(i = 1, 2)$, $\tau_{\text{total}} = \tau_1 + \tau_1' + \tau_2 + \tau_2'$, and B_2 is the second excited band population. Label a for this work, and b for experiment [23].

s_1		τ_1	τ_1'	τ_2	τ_2'	τ_{total}	$B_2(\tau_{\text{total}})$
10	a	24.6	28.8	7.4	2.3	63.1	0.982
	b	24.5	28.8	8.1	2.2	63.6	0.982
20	a	15.0	3.3	2.0	20.7	41	0.991
	b	17.2	25	12.5	1.1	55.8	0.973

and consider the $q = 0$ case. Since dephasing becomes pronounced as the elapsed time gets longer, the proposed excitation method is expected to be of more value for shorter elapsed time. In Table III, label *a* corresponds to our numerical results and *b* to the results in Ref. [23]. In the case of $s_1 = 10$, the two results almost coincide, whereas in the case of $s_1 = 20$, we discovered a scheme more efficient with an even shorter duration than the results of $s_1 = 20$ *b*. This fact reflects the multiple-minimum issue stated in Appendix A.

APPENDIX C: ENERGY BANDS OF AN ATOM IN THE BICHROMATIC LATTICE

In this Appendix, we present a simple treatment of the band structure of the one-dimensional bichromatic lattice. Here we apply the second-order perturbation theory, regarding the second harmonic as the perturber to the monochromatic OL, and explain the crossing features of the bichromatic band structure discussed in Sec. II. The Hamiltonian $H_{B1} = -\frac{\partial^2}{\partial x^2} + s_1 \sin^2(x)$ gives the Bloch states of the noninteracting bosonic atoms. Each Bloch state is expanded as

$$\chi_q^n(x) = e^{iqx} \sum_K C_{B1}(n, q, K) e^{2iKx}, \tag{C1}$$

where the coefficient $C_{B1}(n, q, K)$ derives from the recurrent formula,

$$(q + 2K)^2 C_{B1}(n, q, K) - s_1 C_{B1}(n, q, K - 1)/4 - s_1 C_{B1}(n, q, K + 1)/4 = \left(e_q^n - s_1/2\right) C_{B1}(n, q, K). \tag{C2}$$

Figure 13 is the Strutt diagram which shows E_q^n of Eq. (3) against s_2. The shaded regions pertain to the stable solutions and the counterparts to the unstable ones. The Dirac points mentioned in Sec. II appear at the intersections of the shaded regions, for instance, at $s_2 = (s_1/4)^2 = 6.25$ for the bands labeled first and second, and at $(s_1/12)^2 \simeq 0.694$ for second and third. An additional Dirac point appears at $s_2 = (s_1/8)^2 \simeq 1.56$ corresponding to $q = \pm 1$. The pulse sequence transfers only those atoms near $q = 0$, therefore we focus on $q = 0$ hereafter.

The second-order perturbation theory yields the eigenenergies of the bichromatic OL system,

$$\tilde{E}_q^n \simeq e_q^n + \frac{s_2}{2} - \frac{s_2}{4} d_n + \frac{s_2^2}{16} f_n, \tag{C3}$$

where using the standard formulas

$$d_n = \sum_K \{C_{B1}(n, q, K) C_{B1}(n, q, K + 2) + C_{B1}(n, q, K) C_{B1}(n, q, K - 2)\} \tag{C4}$$

and

$$f_n = \sum_{j \neq n} \frac{\left[\sum_K \{C_{B1}(n, q, K) C_{B1}(n, q, K + 2) + C_{B1}(n, q, K) C_{B1}(n, q, K - 2)\}\right]^2}{\left(e_q^n - e_q^j\right)}. \tag{C5}$$

For the first and second excited bands, the second-order perturbation term can be ignored, thus the lattice height s_2^c which causes the Dirac point is determined by the condition of degeneracy,

$$e_0^1 + \frac{s_2^c}{2} - \frac{s_2^c}{4} d_1 = e_0^2 + \frac{s_2^c}{2} - \frac{s_2^c}{4} d_2,$$

namely

$$s_2^c = \frac{4\left(e_0^2 - e_0^1\right)}{(d_2 - d_1)}. \tag{C6}$$

As for the third and fourth excited bands, the second-order perturbation proves to play a more important role, thus s_2^c for this case is obtained similarly,

$$s_2^c = \frac{2(d_4 - d_3) \pm 2\sqrt{(d_4 - d_3)^2 - 4(f_4 - f_3)\left(e_0^4 - e_0^3\right)}}{(f_4 - f_3)}. \tag{C7}$$

Substituting actual values into the coefficients in Eqs. (C6) and (C7), we discuss the case of the first and second excited bands more closely. Power series for characteristic values being known such as in the section for Mathieu functions in Ref. [42], the relations between the lattice height s_1 and

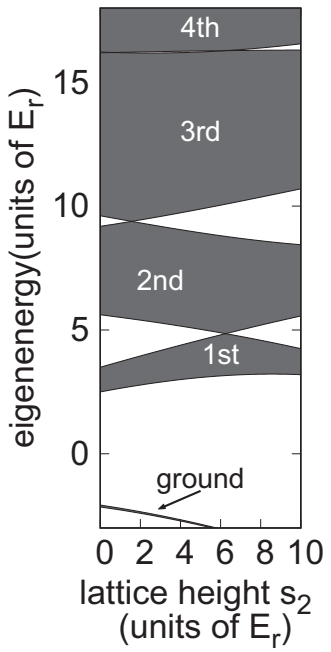

FIG. 13. Stability diagram of the bichromatic lattice with $s_1 = 10$. See text for details.

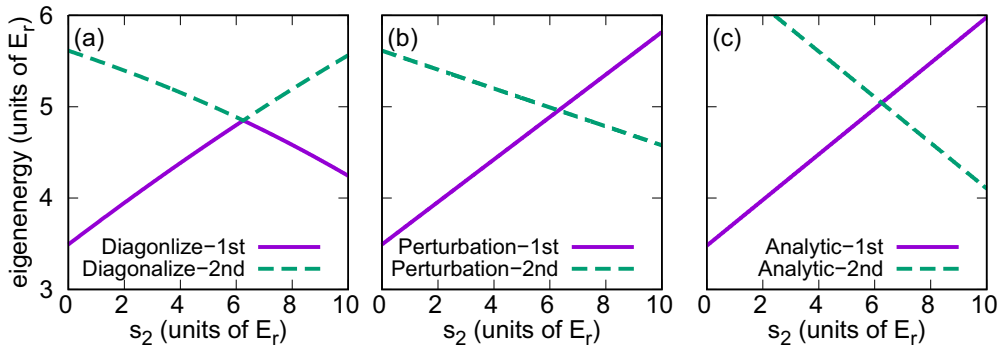

FIG. 14. Eigenenergies for first and second excited bands at $q = 0$ as a function of s_2. In this plot, the eigenenergies are shifted by $(s_1/2 + s_2/2)$. (a), (b) and (c) show the results of exact diagonalization, perturbation theory [Eq. (C3)], and analytic function [Eqs. (C8) and (C9)].

the eigenenergies are found to be $e_0^1 = 4 + \frac{s_1}{2} - \frac{s_1^2}{192}$ and $e_0^2 = 4 + \frac{s_1}{2} + \frac{5s_1^2}{192}$ where $s_1, s_2 \ll 1$. Now that dominant terms in the expansion for eigenfunctions are limited, the Bloch coefficients may be simply approximated by $C_{B1}(1, 0, \pm 1) = \pm\frac{1}{\sqrt{2}}$ for $n = 1$ and $C_{B1}(2, 0, \pm 1) = \frac{1}{\sqrt{2}}$ for $n = 2$, and all the other components are 0. We thus get $d_1 = -1$ and $d_2 = 1$ [Eq. (C8)] so that

$$\tilde{E}_0^1 \simeq 4 + \frac{s_1}{2} + \frac{s_2}{2} - \frac{s_1^2}{192} + \frac{s_2}{4}, \tag{C8}$$

and

$$\tilde{E}_0^2 \simeq 4 + \frac{s_1}{2} + \frac{s_2}{2} + \frac{5s_1^2}{192} - \frac{s_2}{4}. \tag{C9}$$

The crossing point is located at $s_2^c = \frac{s_1^2}{16}$. To confirm the validity of this approximation at $s_1 = 10$, we plot the eigenenergies of the first and second excited bands as a function of s_2 in Fig. 14. The perturbation result agrees well with that of the exact diagonalization for small s_2 and shows the crossing. The analytic formula of the second excited band overestimates the eigenenergy but yields an accurate estimate of s_2 for the crossing.

The eigenenergies of the third and fourth bands of the monochromatic OL are similarly found to be $e_0^3 = 16 + \frac{s_1}{2} + \frac{s_1^2}{480} - \frac{317s_1^4}{2^{16}3^35^3}$ and $e_0^4 = 16 + \frac{s_1}{2} + \frac{s_1^2}{480} + \frac{433s_1^4}{2^{16}3^35^3}$. If we apply the same simple assumption as for the $n = 1$ and 2 bands above, we find d_n goes to 0. Thus, we assume here that the Bloch functions have some components other than $K = \pm 2$. The Bloch coefficients for the third excited band are then given by $C_{B1}(3, 0, \pm 3) = \mp\frac{40-\sqrt{40^2+s_1^2}}{\sqrt{2}s_1}$, $C_{B1}(3, 0, \pm 2) = \pm\frac{1}{\sqrt{2}}$, and $C_{B1}(3, 0, \pm 1) = \pm\frac{24-\sqrt{24^2+s_1^2}}{\sqrt{2}s_1}$ and the other components are 0. For the fourth excited band, the coefficients are $C_{B1}(4, 0, \pm 3) = -\frac{40-\sqrt{40^2+s_1^2}}{\sqrt{2}s_1}$, $C_{B1}(4, 0, \pm 2) = \frac{1}{\sqrt{2}}$, $C_{B1}(4, 0, \pm 1) = \frac{24-\sqrt{24^2+s_1^2}}{\sqrt{2}s_1}$, and $C_{B1}(4, 0, 0) = \frac{(8-\sqrt{8^2+s_1^2})(24-\sqrt{24^2+s_1^2})}{2\sqrt{2}s_1^2}$, and the other components are 0. These values give an approximate formula $d_4 - d_3 \simeq \frac{5s_1^2}{2^8 3^2}$. For the second-order perturbation term, we apply the simple assumption used for the first and second excited bands, such as $C_{B1}(0, 0, 0) = 1$, $C_{B1}(3, 0, \pm 2) = \pm\frac{1}{\sqrt{2}}$, $C_{B1}(4, 0, \pm 2) = \frac{1}{\sqrt{2}}$, and $C_{B1}(7, 0, \pm 4) = \pm\frac{1}{\sqrt{2}}$, $C_{B1}(8, 0, \pm 4) = \frac{1}{\sqrt{2}}$, and the other components are set to 0. The corresponding energies are $e_0^0 = 0$, $e_3^0 = e_4^0 = 16$, and $e_7^0 = e_8^0 = 64$, leading to $f_4 - f_3 = 1/8$. The analytic expressions are thus given by

$$\tilde{E}_0^3 = e_0^3 + \frac{s_2}{2} + \frac{11s_1^2 s_2}{2^{10}3^25} - \frac{s_2^2}{2^8 3^2}, \tag{C10}$$

and

$$\tilde{E}_0^4 = e_0^4 + \frac{s_2}{2} - \frac{14s_1^2 s_2}{2^{10}3^25} + \frac{5s_2^2}{2^8 3^2}. \tag{C11}$$

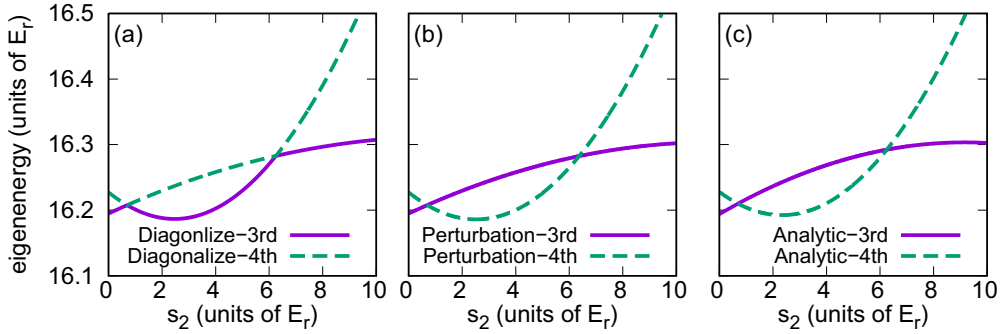

FIG. 15. Eigenenergies for the third and fourth excited bands at $q = 0$ as a function of s_2 as in Fig. 14.

Finally, we obtain $s_2^c = \frac{5s_1^2}{2^4 3^2} \pm \frac{4s_1^2}{2^4 3^2}$. Consequently, the first crossing point is given by $\frac{s_1^2}{144}$ and the second crossing point is given by $\frac{s_1^2}{16}$. Figure 15 shows the s_2 dependence of the eigenenergies of the third and fourth excited bands. Again, the results of the perturbation theory and the analytic formula both show a good agreement with that of the exact diagonalization.

We surmise that the crossing points may be represented by a series of $(\frac{s_1}{4l})^2$ where l is an odd integer for $q = 0$, and $(\frac{s_1}{4k})^2$ where k is an even integer for $q = \pm 1$ to this order. It may be interesting to work out mathematical details to clarify the origin and significance of this behavior. We numerically checked the results up to $s_1 = 100$. It may be conjectured that the mathematical features found here hold up to all orders.

[1] O. Morsch and M. Oberthaler, Rev. Mod. Phys. **78**, 179 (2006); P. Windpassinger and K. Sengstock, Rep. Prog. Phys. **76**, 086401 (2013), and references therein.

[2] J. Dalibard, F. Gerbier, G. Juzeliūnas, and P. Öhberg, Rev. Mod. Phys. **83**, 1523 (2011), and references therein.

[3] A. Eckardt, Rev. Mod. Phys. **89**, 011004 (2017) and references therein.

[4] X. Li and W. Vincent Liu, Rep. Prog. Phys. **79**, 116401 (2016), and references therein.

[5] F. Damon, F. Vermersch, J. G. Muga, and D. Guéry-Odelin, Phys. Rev. A **89**, 053626 (2014).

[6] S. Masuda, K. Nakamura, and A. del Campo, Phys. Rev. Lett. **113**, 063003 (2014); S. Martínez-Garaot, M. Palmero, J. G. Muga, and D. Guéry-Odelin, Phys. Rev. A **94**, 063418 (2016).

[7] A. Görlitz, T. Kinoshita, T. W. Hänsch, and A. Hemmerich, Phys. Rev. A **64**, 011401(R) (2001); M. Weitz, G. Cennini, G. Ritt, and C. Geckeler, *ibid.* **70**, 043414 (2004); G. Ritt, C. Geckeler, T. Salger, G. Cennini, and M. Weitz, *ibid.* **74**, 063622 (2006).

[8] T. Salger, C. Geckeler, S. Kling, and M. Weitz, Phys. Rev. Lett. **99**, 190405 (2007).

[9] T. Salger, G. Ritt, C. Geckeler, S. Kling, and M. Weitz, Phys. Rev. A **79**, 011605(R) (2009).

[10] S. Kling, T. Salger, C. Grossert, and M. Weitz, Phys. Rev. Lett. **105**, 215301 (2010).

[11] D. Witthaut, T. Salger, S. Kling, C. Grossert, and M. Weitz, Phys. Rev. A **84**, 033601 (2011).

[12] T. Salger, C. Grossert, S. Kling, and M. Weitz, Phys. Rev. Lett. **107**, 240401 (2011).

[13] L. Mazza, A. Bermudez, N. Goldman, M. Rizzi, M. Angel Martin-Delgado, and M. Lewenstein, New J. Phys. **14**, 015007 (2012); X. Lopez-Gonzalez, J. Sisti, G. Pettini, and M. Modugno, Phys. Rev. A **89**, 033608 (2014).

[14] L. Fallani, J. E. Lye, V. Guarrera, C. Fort, and M. Inguscio, Phys. Rev. Lett. **98**, 130404 (2007); Shi-Liang Zhu, Z.-D. Wang, Y.-H. Chan, and L.-M. Duan, *ibid.* **110**, 075303 (2013); Y. He, K. Wright, S. Kouachi, and Chih-Chun Chien, Phys. Rev. A **97**, 023618 (2018).

[15] D. Witthaut, F. Trimborn, V. Kegel, and H. J. Korsch, Phys. Rev. A **83**, 013609 (2011); S. Nascimbene, N. Goldman, N. R. Cooper, and J. Dalibard, Phys. Rev. Lett. **115**, 140401 (2015).

[16] B. Reid, M. Moreno-Cardoner, J. Sherson, and G. De Chiara, Phys. Rev. A **94**, 063629 (2016).

[17] J. F. Sherson, S. J. Park, P. L. Pedersen, N. Winter, M. Gajdacz, S. Mai, and J. Arlt, New J. Phys. **14**, 083013 (2012); P. L. Pedersen, M. Gajdacz, N. Winter, A. J. Hilliard, J. F. Sherson, and J. Arlt, Phys. Rev. A **88**, 023620 (2013).

[18] J. Heinze, J. S. Krauser, N. Fläschner, B. Hundt, S. Götze, A. P. Itin, L. Mathey, K. Sengstock, and C. Becker, Phys. Rev. Lett. **110**, 085302 (2013).

[19] T. Yamakoshi and S. Watanabe, Phys. Rev. A **91**, 063614 (2015).

[20] T. Yamakoshi, S. Watanabe, S. Ohgoda, and A. P. Itin, Phys. Rev. A **93**, 063637 (2016).

[21] T. Yamakoshi, F. Saif, and S. Watanabe, Phys. Rev. A **97**, 023620 (2018).

[22] N. Fläschner, M. Tarnowski, B. S. Rem, D. Vogel, K. Sengstock, and C. Weitenberg, Phys. Rev. A **97**, 051601(R) (2018).

[23] Y. Zhai, X. Yue, Y. Wu, X. Chen, P. Zhang, and X. Zhou, Phys. Rev. A **87**, 063638 (2013).

[24] J. Hecker Denschlag, J. E. Simsarian, H. Häffner, C. McKenzie, A. Browaeys, D. Cho, K. Helmerson, S. L. Rolston, and W. D. Phillips, J. Phys. B: At. Mol. Opt. Phys. **35**, 3095 (2002).

[25] Z. Wang, B. Yang, D. Hu, X. Chen, H. Xiong, Biao Wu, and Xiaoji Zhou, Phys. Rev. A **94**, 033624 (2016).

[26] X. Zhou, S. Jin, and J. Schmiedmayer, New J. Phys. **20**, 055005 (2018).

[27] D. Hu, L. X. Niu, S. J. Jin, X. Z. Chen, G. J. Dong, J. Schmiedmayer, and X. J. Zhou, Commun. Phys. **1**, 29 (2018).

[28] D. J. Tannor, *Introduction to Quantum Mechanics* (University Science Books, Herndon, VA, 2007).

[29] B. Yang, S. Jin, X. Dong, Zhe Liu, Lan Yin, and Xiaoji Zhou, Phys. Rev. A **94**, 043607 (2016).

[30] M. Machholm, C. J. Pethick, and H. Smith, Phys. Rev. A **67**, 053613 (2003).

[31] Y. Zhang and B. Wu, Phys. Rev. Lett. **102**, 093905 (2009).

[32] D. Hu, L. Niu, B. Yang, Xuzong Chen, Biao Wu, Hongwei Xiong, and Xiaoji Zhou, Phys. Rev. A **92**, 043614 (2015).

[33] M. Olshanii, Phys. Rev. Lett. **81**, 938 (1998).

[34] Cheng Chin, R. Grimm, P. Julienne, and E. Tiesinga, Rev. Mod. Phys. **82**, 1225 (2010)

[35] C. Kittel, *Introduction to Solid State Physics*, 8th ed. (Wiley, New York, 2004).

[36] S. J. Park, H. K. Andersen, S. Mai, J. Arlt, and J. F. Sherson, Phys. Rev. A **85**, 033626 (2012).

[37] Yan Chen, Li-Bin Fu, and Yong Chen, Physica A **390**, 1033 (2011).

[38] Lei Wang, M. Troyer, and X. Dai, Phys. Rev. Lett. **111**, 026802 (2013); S. Nakajima, T. Tomita, S. Taie, T. Ichinose, H. Ozawa, Lei Wang, M. Troyer, and Y. Takahashi, Nat. Phys. **12**, 296 (2016); M. Lohse, C. Schweizer, O. Zilberberg, M. Aidelsburger, and I. Bloch, *ibid.* **12**, 350 (2016).

[39] M. Holthaus, J. Phys. B: At. Mol. Opt. Phys. **49**, 013001 (2016).

[40] For example, W. S. Bakr, P. M. Preiss, M. Eric Tai, R. Ma, J. Simon, and M. Greiner, Nature **480**, 500

(2011); M. Łącki and J. Zakrzewski, Phys. Rev. Lett. **110**, 065301 (2013).

[41] For example, C. V. Parker, Li-Chung Ha, and Cheng Chin, Nat. Phys. **9**, 769 (2013); Wei Zheng and Hui Zhai, Phys. Rev. A **89**, 061603(R) (2014); Li-Chung Ha, Logan W. Clark, C. V. Parker, B. M. Anderson, and Cheng Chin, Phys. Rev. Lett. **114**, 055301 (2015).

[42] *Handbook of Mathematical Functions with Formulas, Graphs, and Mathematical Tables*, edited by M. Abramowitz and I. A. Stegun (Dover, New York, 1972).